

Discerning the effect of various irradiation modes on the corrosion of Zircaloy-4

Peng Wang^{a,*}, Bruce Kammenzind^b, Richard Smith^b, Arthur Motta^c, Matthieu Aumand^d, Damien Kaczorowski^e, Mukesh Bachhav^f, Gary Was^a

^a Nuclear Engineering and Radiological Sciences, University of Michigan, Ann Arbor, MI 48109, USA

^b Naval Nuclear Laboratory, Bettis Laboratory, PO box 79, West Mifflin, PA 15122, USA

^c Ken and Mary Alice Lindquist Department of Nuclear Engineering, Pennsylvania State University, University Park, PA 16802, USA

^d Framatome Inc., Old Forest Road, Lynchburg, VA 24501, USA

^e Framatome, 2 Rue du Professeur Jean Bernard, Lyon 69007, France

^f Idaho National Laboratory, Materials and Fuel Complex, Idaho Falls, ID, USA

ARTICLE INFO

Keywords:
Zirconium
Corrosion
Irradiation
Radiolysis

ABSTRACT

Using proton irradiation, this study investigates the individual influence of several factors on the corrosion kinetics of Zircaloy-4 in a hydrogenated water environment simulating a Pressurized Water Reactor (PWR). Using both simultaneous irradiation-corrosion and autoclave corrosion, we separately examine (i) the effect of pre-irradiation on modifying the structure of the material, (ii) the impact of irradiation on creating defects in the growing oxide layer during corrosion, and (iii) the influence of irradiation on increasing the corrosion potential through radiolysis during corrosion. To replicate the neutron-irradiated microstructure, two proton pre-irradiation schedules were employed: Schedule 1 (isothermal irradiation at 350 °C to 5 dpa) to simulate high-temperature PWR conditions, and Schedule 2 (two-step process: irradiation to 2.5 dpa at -10 °C followed by 2.5 dpa at 350 °C) to simulate lower temperature PWR and Boiling Water Reactor (BWR) conditions. Long-term autoclave corrosion testing for 360 days at 320 °C revealed no significant difference between unirradiated samples and those pre-irradiated according to either schedule, with all samples exhibiting sub-cubic kinetics within the pre-transition regime. Pre-irradiated samples underwent Simultaneous Irradiation Corrosion (SIC) tests, corroding in 320 °C water while being irradiated with protons. Corrosion was found to accelerate in all SIC-tested samples relative to autoclave conditions, with the greatest increase observed in non-pre-irradiated regions of the samples. Pre-irradiation with either schedule resulted in a slower corrosion rate compared to non-pre-irradiated regions under SIC conditions. The degree of radiolysis observed in the SIC tests surpassed typical PWR conditions, approaching levels found in BWRs. Radiolysis products were identified as a primary contributors to accelerated corrosion, corroborated by radiolysis bar tests. These findings underscore the intricate interactions between irradiation, corrosion, and water chemistry in determining Zircaloy-4 corrosion kinetics within nuclear reactor environments.

1. Introduction

The corrosion kinetics of Zr alloys under light water reactor (LWR) conditions have been described as consisting of a pre-transition regime, in which corrosion kinetics are governed by a parabolic or sub-parabolic rate law, and a post-transition regime, where spatially out-of-phase cyclic transitions produce nearly linear corrosion kinetics [1–6]. It is also well known that post-transition corrosion of the Zircaloy family of alloys

under irradiation occurs at a faster rate than in autoclaves [7,8]. Various causes have been suggested for this acceleration of corrosion in-service relative to autoclave testing, including changes to the metal microstructure caused by displacement damage, changes to the oxide properties through the creation of defects while under irradiation, an increase in radiolytic species in the water, and the presence of a hydride rim due to the temperature gradient present in service [9].

Kammenzind et al. reported the long-term in-reactor corrosion

* Corresponding author.

E-mail address: wpf@umich.edu (P. Wang).

<https://doi.org/10.1016/j.jnucmat.2024.155505>

Received 13 August 2024; Received in revised form 22 October 2024; Accepted 7 November 2024

Available online 8 November 2024

0022-3115/© 2024 Elsevier B.V. All rights reserved, including those for text and data mining, AI training, and similar technologies.

behavior of non-fueled Zircaloy-4 samples in the Advanced Test Reactor (ATR) under isothermal corrosion at temperatures ranging from 270 °C to 320 °C and constant neutron flux conditions in PWR water chemistry [10]. The data indicate that Zircaloy-4 corrosion kinetics are unaffected (or minimally affected) by the PWR radiation environment during the pre-transition regime, but during longer exposures, a significant acceleration in corrosion rate was observed relative to out-of-pile samples.

As described in detail in [10,11], these observations led to the hypothesis that the following three mechanisms acting synergistically can lead to the significant in-PWR corrosion acceleration in the post-transition corrosion rates of Zircaloy-4 relative to corrosion in autoclave:

1. Heterogeneous radiolysis occurs within the outer porous oxide layers of a Zircaloy-4 post-transition corrosion film (whether it is formed in-reactor or first formed out-of-reactor in an autoclave), resulting in the local production of a more oxidizing corrosion environment at the outer surface of the passivating oxide layer than in the bulk water channels of a PWR.
2. A photovoltaic effect occurs on the n-type semiconducting, inner passivating zirconium oxide layer at the metal oxide interface, increasing the electron-hole density at the outer surface of the passivating layer that causes photo-induced dissolution and degrades the mechanical stability of the oxide layer [11].
3. Accumulated neutron irradiation effects in the microstructure and microchemistry of the Zircaloy-4 metal result in the formation of dislocation loops and redistribution of alloying elements. The inner passivating corrosion layer generated from the pre-irradiated metal matrix further enhances the n-type semiconducting nature of the inner passivating layer and its photo-induced dissolution.

In this study, proton pre-irradiated samples [12] were exposed in an autoclave for 360 days and in a set of simultaneous irradiation-corrosion (SIC) tests for a shorter period (3 days). Both corrosion tests were performed at 320 °C. The microstructure and microchemistry of the Zircaloy-4 samples following proton pre-irradiation have been thoroughly characterized and analyzed in a previous publication [12]. The long-term autoclave exposure was conducted to elucidate the separate effects of accumulated irradiation damage and microchemical changes to the Zircaloy-metal alone (outside of a radiation environment) on corrosion of Zircaloy-4 in a PWR water chemistry environment. The short-term SIC tests were performed to elucidate the effects of irradiation on Zircaloy-4 corrosion under the following conditions: (1) exposure of Zircaloy-4 with/without pre-irradiation; (2) exposure of Zircaloy-4 with/without pre-irradiation under simultaneous displacement damage in the metal and the oxide, and radiolysis in the water; (3) exposure of pre-irradiated Zircaloy-4 only to radiolysis in the water.

2. Experimental

2.1. Materials

Fully recrystallized Zircaloy-4 in 1 mm sheet stock provided by Naval Nuclear Laboratories (NNL) was processed for PWR corrosion resistance in the single alpha-phase field, with final recrystallization anneals in the high alpha-phase following rolling [10,11,13], producing an equiaxed grain size of $\sim 12 \mu\text{m}$ and a mean Laves phase precipitate size of $\sim 0.2 \mu\text{m}$ (Table 1).

Electric discharge machining (EDM) was used to create both matchstick-size bar samples with a geometry of $2 \times 18 \times 1 \text{ mm}$ and disc

samples with a diameter of 7.6 mm from the sheet stock. EDM was applied to the sample edges only. The EDM process affected only the first 100 μm from the surface. The primary corrosion surfaces were far from that region and were not affected by EDM. The 7.6 mm diameter discs were ground down to 110 μm in thickness, followed by mechanical grinding and polishing to a mirror finish using silicon carbide paper and diamond paste, followed by chemical-mechanical polishing with colloidal silica particles of 50 nm size to remove any surface deformation layer. The polished samples were ultrasonically cleaned first in organic solvent and then in deionized water for at least 15 min and air dried. In all cases, the primary corrosion surfaces represent the original sheet planar surface orientation, which were also the surfaces that were pre-irradiated.

2.2. Proton pre-irradiation

As mentioned above, two proton pre-irradiation schedules were used on the Zircaloy-4 bar and disc samples:

Schedule 1: isothermal irradiation at 350 °C to 5 dpa, and

Schedule 2: a two-step (2ST) irradiation sequence consisting of irradiation at $-10 \text{ }^\circ\text{C}$ to 2.5 dpa followed by irradiation at 350 °C to 2.5 dpa.

As discussed in detail in [12], both the Schedule 1 and the Schedule 2 irradiation produced damage to the Zr matrix similar to that seen in reactor-irradiated samples. However, the Schedule 1 irradiation sequence resulted in minimal precipitate amorphization and Fe redistribution. The Schedule 2 irradiation was designed to induce second-phase precipitate (SPP) amorphization during the low-temperature step, with the subsequent high-temperature step aimed at creating displacement damage to redistribute Fe from the amorphized SPP into the matrix without recrystallizing the SPPs. The Schedule 1 irradiation sequence best approximates the microstructure resulting from neutron irradiation of Zircaloy-4 in a PWR at irradiation temperatures of approximately 330 to 360 °C [14]. The Schedule 2 (two-step) irradiation sequence best approximates neutron irradiation effects on the Zircaloy microstructure occurring in lower temperature PWRs and BWRs (260–310 °C) [14]. The experimental matrix is given in Table 2. By pre-irradiating the samples and subjecting only well-defined regions to in-situ corrosion, the separate effects of each pre-irradiation process on the corrosion response can be discerned.

As previously described, the 2 MeV proton pre-irradiations were conducted using the 3 MV NEC Pelletron accelerator at the Michigan Ion Beam Laboratory (MIBL) [12]. The proton beam current density was 41 $\mu\text{A}/\text{cm}^2$ (2.6×10^{14} protons/ $\text{cm}^2 \cdot \text{s}$), which corresponds to a damage rate in the metal of 1.65×10^{-5} dpa/s, or roughly two orders of magnitude higher than peak damage rates experienced from neutron irradiation in a PWR environment. The bar samples were pre-irradiated exclusively in a $3 \times 2 \text{ mm}$ section at the center, while the rest of the sample surfaces were considered unirradiated. For the disc samples, irradiation was applied to either a quarter (Schedule 1) or half (Schedule 2) of the surface, with the remaining area considered unirradiated.

The SRIM plot in Fig. 1 shows the 2 MeV proton energy penetration depth into zirconium. The damage profile for the first 10 μm of metal below the surface is relatively uniform. The proton irradiation dose was calculated at a depth of 3–5 μm below the irradiated surface, corresponding to a standard focused ion beam (FIB) lift-out sampling depth for microstructural investigation. At 5 dpa, the predicted proton fluence is 7.8×10^{19} protons/ cm^2 . These conditions were targeted to ensure

Table 1

Chemical composition of recrystallized Zircaloy-4 (wt%) used in this study.

Alloy	Sn	O	Si	Al	N	C	Cr	Fe	Zr
Zircaloy-4	1.55	0.14	0.01	0.003	0.002	0.016	0.11	0.22	Bal.

Table 2
Matrix of exposure experiments for the pre-irradiated (5 dpa) Zircaloy-4 samples.

Experiments	Materials	Sample Designation #	Objective
Long-term 320 °C Autoclave Exposures (A)	Zircaloy-4 bars (18 × 2 × 1 mm)	Unirradiated	Baseline corrosion
		Schedule 1: #350-A	Effect of Pre-irradiation Schedule 1 on corrosion
Simultaneous Irradiation-Corrosion Experiments (SIC) At 320 °C	Zircaloy-4 discs (7.6 mm disc)	Schedule 2: #2ST-A	Effect of Pre-irradiation Schedule 2 on corrosion
		Unirradiated	Baseline corrosion
		Schedule 1: #350-SIC	Effect of microstructural changes in the metal and oxide during irradiation and radiolysis on the corrosion behavior of Schedule 1 samples
		Schedule 2: #2ST-SIC	Effect of microstructural changes in the metal and oxide during irradiation and radiolysis on the corrosion behavior of Schedule 2 samples
Radiolysis Bar Study (R) at 320 °C	Zircaloy-4 foil (2 × 1 × 0.1 mm)	Schedule 1: 350-R-bar	Effect of radiolysis only on Schedule 1 pre-irradiation sample corrosion
		Schedule 2: 2ST-R-bar	Effect of radiolysis only on Schedule 2 pre-irradiation sample corrosion

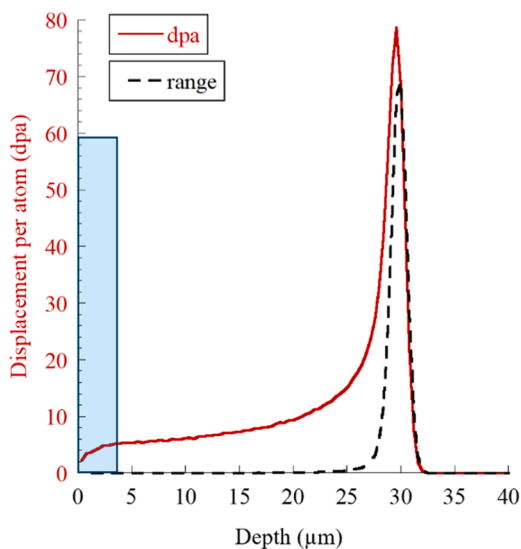


Fig. 1. SRIM simulated proton range probability and damage profile for 2 MeV protons in Zr. This calculation was done using the Quick Kinchin-Pease option of SRIM 2008 [15], with the displacement energy of 40 eV, and assuming a proton fluence of 7.8×10^{19} protons/cm². The boxed region shows the maximum advancement of the oxide layer for the corrosion exposures in this study.

subsequent corrosion exposures will only be corroding the irradiated metal in which the damage level is approximately uniform. The depth range of analysis is selected assuming that corrosion consumes $< 3 \mu\text{m}$ of metal and generates an oxide layer $< 5 \mu\text{m}$ thick after post-irradiation autoclave exposure for 360 days.

2.3. Post-irradiation long-term autoclave exposure

Post-irradiation autoclave corrosion testing was performed to distinguish between the specific impacts of pre-existing damage to the metal alone and of simultaneous irradiation-corrosion in which water

radiolysis and active displacement damage can play a role. Post-irradiation autoclave corrosion testing was performed in the High-Temperature Corrosion Laboratory at the University of Michigan. The exposures took place in a 316L stainless steel autoclave containing pure water with 3 wt. ppm dissolved hydrogen at 320 °C, at 13.8 MPa (2000 psi). The autoclave was opened periodically to access the corroded sample and to determine oxide thickness and corrosion kinetics via SEM/FIB analysis at various stages.

2.4. Simultaneous irradiation-corrosion (SIC) experiment

Simultaneous irradiation-corrosion experiments were conducted on the pre-irradiated Zircaloy-4 disc samples and radiolysis bar samples (Table 2) in contact with 320 °C pure water with 3 wt. ppm dissolved hydrogen gas and a conductivity of $< 0.1 \mu\text{S}/\text{cm}$ using the facility described in [16]. Protons are accelerated to 5.4 MeV in a 3 MV NEC Pelletron and pass through the 110 μm thick Zircaloy-4 disc sample into the water circulating through a mini-autoclave corrosion cell (Fig. 2) [16–18]. The Zircaloy-4 disc serves both as the sample on which corrosion measurements were made, and as the window between the high vacuum of the beamline and the high-temperature, high-pressure water in the cell. A proton flux of 1.69×10^{12} protons/(cm²s) (corresponding to a current density of 270 nA/cm² and a damage rate of 1×10^{-7} dpa/s) was used in these SIC experiments to a fluence of 4.39×10^{17} protons/cm², equivalent to a damage level of 0.026 dpa over 72 h at the Zircaloy-4 sample surface in contact with the water. Because this increment in dose over the pre-irradiated damage to the metal is relatively small ($\sim 1\%$), it is neglected here. The SIC damage rate is approximately the same as obtained during neutron irradiation on Zr at a neutron flux of 1×10^{14} neutrons/cm²s in PWR.

2.5. Radiolysis bar

A radiolysis bar aligned parallel to the beam was included in the SIC test to ascertain the separate effect of radiolysis on corrosion, as shown in Fig. 2b. The radiolysis bar sample is positioned in front of the disc on the waterside, with the pre-irradiated surface facing downwards, parallel to the proton beam. Because the bar is placed parallel to the proton beam, the beam does not interact directly with the radiolysis bar sample, but rather only through the water radiolysis products generated in the path of the proton beam. The linear energy transfer (LET) to the water of approximately 6×10^{-11} J/cm per proton translates into a dose rate of ~ 72 kGy/s for a proton energy of 2.04 MeV as it emerges from the Zircaloy-4 foil and enters the water. This dose rate to the water is approximately seven times higher than the maximum dose rate in light water reactor cores, estimated to be about 10 kGy/s [19]. A detailed description of the experimental setup for the simultaneous proton irradiation-corrosion facility has been published elsewhere [16], along with other research activities related to the accelerated corrosion of Zr under proton irradiation [18,20,21].

2.6. Microstructure characterization

2.6.1. Pre-irradiated samples

A detailed description of the effect of the two proton pre-irradiation schedules on the microstructure of Zircaloy-4 is provided in Ref. [12]. This description agrees with overall neutron irradiation observations [22] and is briefly summarized here. Dislocation loops were imaged in STEM bright-field (BF) mode using a Thermo Fisher Scientific TF30 microscope. BF-STEM images were obtained on the $<11\bar{2}0>$ zone axis.

Schedule 1 pre-irradiation (isothermal proton irradiation to 5 dpa at 350 °C) produces $\langle a \rangle$ and $\langle c \rangle$ type dislocation loops in the Zr matrix similar to those observed under neutron irradiation at similar temperatures and dpa levels [22–26]. The dislocation microstructures observed in isothermally pre-irradiated samples increased the hardness of the sample, generally consistent with measurements performed on neutron

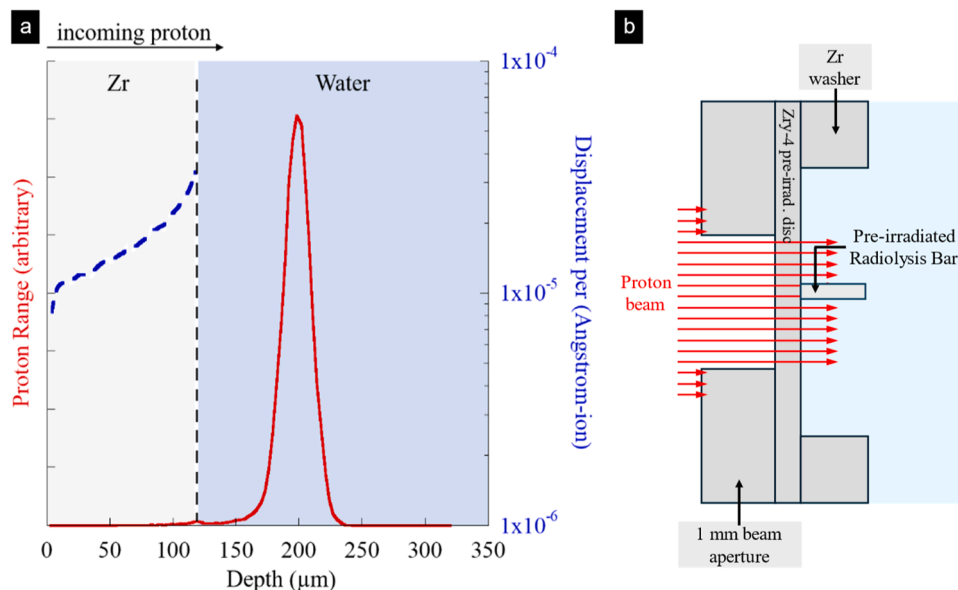


Fig. 2. Illustration of (a) SRIM simulated proton range and displacement rate plot for a 120 μm Zr sample irradiated with 5.4 MeV protons at 320 °C in water and (b) position of the radiolysis bar sample concerning the pre-irradiated Zr foil sample during the SIC experiment.

irradiated samples [24,27]. Although the same amorphization morphology was observed in proton as in neutron irradiation (precipitates with a crystalline core and an amorphous outer layer), the rate of advancement of the amorphous layer during ion irradiation (in nm/dpa) was much lower than the rate seen under neutron irradiation [28]. Consistent with neutron irradiation, Fe redistribution from the very thin amorphous zones that did form was observed [28,29].

In contrast, the Schedule 2 pre-irradiation (two-step proton irradiation) sequence produced complete amorphization of the SPPs and significant Fe depletion [12]. The alignment of $\langle a \rangle$ -loops in the matrix and the formation of Fe-rich rafts near the SPPs after the two-step irradiation sequence were also noted, similar to what was seen in neutron irradiated samples. Based on these observations, we concluded that the two-step proton pre-irradiation process best represents irradiation effects on Zircaloy-4 metal irradiated in all but a very high temperature in a PWR environment.

2.6.2. Post-exposure oxides

Focused ion beam (FIB) trenching was performed on autoclave corroded samples at each opening interval. Two 30-micron trenches were typically milled into the surface of the bar sample using a gallium beam, and the oxide cross-section was then imaged at a tilt of 52° in high-resolution mode on a Thermo Fisher Scientific Helios 650 SEM/FIB. The images were processed using Python code to generate a binary image profile representing the oxide thickness. The total oxide area was calculated, tilt corrected, and divided by the 30 μm trench length to determine the average oxide thickness. The same procedure was applied for oxide thickness measurement using TEM. Thickness variations were calculated from the oxide thickness profile and used as error bars.

TEM liftout samples were also prepared using the same SEM/FIB and subsequently thinned to electron transparency at cryogenic temperature (−150 °C) using a cold stage (Quorum PP3006). The post-exposure oxide samples were characterized using the FEI Talos F200X scanning/transmission electron microscope (S/TEM) equipped with bright field (BF), annular dark field (ADF), high-angle annular dark field (HAADF) detectors, and high-count-rate energy-dispersive x-ray spectroscopy (EDS) at the Michigan Center for Materials Characterization (MC²). The collected EDS dataset was processed into weight and atomic percentages for quantitative analysis using the Velox software package, employing the Brown-Powell ionization cross-section model. At least two 15 μm-long TEM liftout samples were prepared for each condition.

3. Results

3.1. Long-term autoclave exposure on Zircaloy-4

Samples subjected to both Schedule 1 (350 °C isothermal pre-irradiation) and Schedule 2 (two-step pre-irradiation process) were corroded in an autoclave for up to 360 days at 320 °C. The corrosion kinetics of Zircaloy-4 have been extensively studied over the past few decades, either in autoclaves (unirradiated) or in reactors, mostly via weight gain measurements at different exposure intervals [10,30–33]. Because the incomplete coverage of the pre-irradiated region on the samples in this study precluded weight gain measurement, the extent of oxidation was tracked by measuring the oxide thickness in the region of interest as described in the previous section. Fig. 3 shows the corrosion kinetics of both unirradiated region (UR) and pre-irradiated region (IR) for (both Schedule 1: 350 °C and Schedule 2: 2ST) Zircaloy-4 over an exposure time of 360 days.

Sub-cubic corrosion kinetics were observed, characterized by an initially fast corrosion rate lasting for the first ~15 days, followed by a slower growth rate. Both the pre-irradiated and un-irradiated portions of the sample behaved similarly on each bar sample, with only subtle differences between the Schedule 1 (350 °C) and the Schedule 2 (2ST) irradiated samples. These differences were likely caused by sample-to-sample or location-to-location variations rather than any systematic

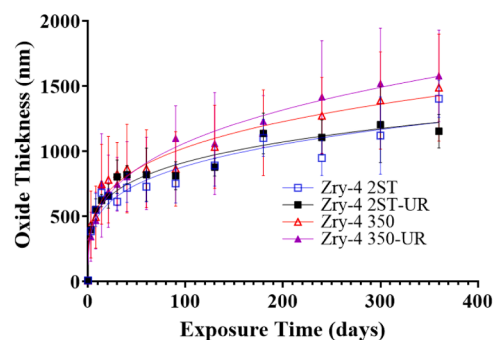


Fig. 3. Corrosion kinetics of Zircaloy-4 treated with and without pre-irradiation. Unirradiated samples were subjected to the same heat treatment but without irradiation.

effect from differing irradiation conditions.

The long-term autoclave corrosion samples agree well with the out-of-pile corrosion data in the literature, within experimental error. The samples show typical pre-transition kinetics with a sub-parabolic rate law, which can be expressed as:

$$d = k \cdot t^n$$

where δ is the oxide thickness, k is the kinetic rate constant, and t is time in days. The n exponent for the pre-irradiated and un-irradiated Zircaloy-4 was in the range 0.25–0.3 in this study, somewhat higher than previously determined values of 0.21–0.24 for Zircaloy-4 and other Laves-phase bearing alloys corroded in an autoclave at 360 °C [34]. For Zircaloy-4, one would expect the oxide transition to occur at about 30 mg/dm² (~ 2 μm) at 316 °C [35], which was not reached in the 360-day exposure. Hence, no kinetic transition nor post-transition corrosion kinetics were observed in this study. This is expected since the in-reactor pre-transition behavior of Zircaloy-4 in a PWR environment shows little deviation from out-of-reactor behavior [10].

The microstructure of the oxide films formed on these samples consisted of columnar grains oriented perpendicular to the metal-oxide interface, as seen in Ref. [2]. Fig. 4 shows the overall appearance of an oxide layer formed on Schedule 2 pre-irradiated (2ST) Zircaloy-4 after 360 days of exposure. Equiaxed grains within the columnar structure were observed in some portions of the oxide, especially near any lateral cracks.

Fig. 5 shows low magnification bright field TEM micrographs of oxide layers formed on Zircaloy-4 at different stages of autoclave corrosion, from 3 to 360 days. The oxide layer formed on the Schedule 2 pre-irradiated sample (#2ST-A) shows a mostly uniform thickness with little undulation at the metal/oxide interface. Although in a few locations, corrosion occurs preferentially in one grain over the next, as shown in the lower right bottom of Fig. 5, these instances were infrequent. In the un-irradiated region, crystalline SPPs were observed at the metal/oxide interface, showing delayed oxidation and a crescent-shaped crack on top of the SPP (e.g., Schedule 2 #2ST-A, UR region for 60 days exposure) as typically observed in the literature [10,20,36]. Isolated hydrides were observed in some regions of the grain interior (e.g., Schedule 2 #2ST-A, IR region for 360 days exposure), typically originating from the metal/oxide interface and extending into the matrix. Minor lateral cracks were found in the oxide layer, mostly associated with the presence of equiaxed grains [37] or SPPs. There was no significant difference in overall oxide morphology between the pre-irradiated and non-pre-irradiated regions for either pre-irradiation Schedule. Fig. 5 shows TEM micrographs of these samples, separated by the pre-irradiation schedule, comparing in each case the microstructure of the oxide formed on the regions subjected to pre-irradiation

versus those that were not.

Fig. 5 shows that the Schedule 1 isothermally pre-irradiated sample (#350-A, 5 dpa) exhibited a somewhat greater propensity to develop lateral cracks throughout the thickness of the oxide compared to Schedule 2 samples. Some regions experienced enhanced localized corrosion, resulting in nodule-like oxide formation accompanied by extensive cracking, usually associated with grain boundaries and surface particles likely introduced during sample preparation. Cracking is more frequent in the unirradiated portion of the sample and is mostly observed in the outer part of the oxide. These are believed to be artifacts of sample preparation and were only seen in the Schedule 1 sample (#350-A).

Fig. 6 shows that roughly the same irradiation damage can still be observed after 360 days of autoclave exposure at 320 °C. The long-term autoclave exposure corrosion tests demonstrate that the amorphized SPPs produced by the two-step pre-irradiation remain amorphous after the corrosion test. The preservation of the as-irradiated microstructure in the corroded samples indicates that the corrosion temperature did not significantly modify the microstructure and microchemical changes introduced by proton pre-irradiation.

Fig. 7 shows the microstructure differences between unirradiated and pre-irradiated Zr substrates. In the unirradiated matrix, long, tangled dislocation networks are observed, while well-distributed and aligned $\langle a \rangle$ -loops are present in the pre-irradiated Zr substrate. Additional observations, such as SPP amorphization after Schedule 2 irradiation and raft formation around SPPs, further confirm the effects of irradiation. More extensive microstructural characterization can be found in the previous publication [12].

3.2. Simultaneous irradiation-corrosion (SIC) experiments

SIC experiments were performed on pre-irradiated zirconium disc samples. The SIC region is centrally located on the sample in a circular shape, encompassing both the pre-irradiated and unirradiated regions, as illustrated in Fig. 8. The corrosion region that developed during the SIC experiment was further divided into four regions: the unirradiated region outside of the SIC condition (UR), the unirradiated region under SIC condition (UR-SIC), the pre-irradiated region outside of the SIC condition (PR), and the pre-irradiated region under SIC condition (PR-SIC). On the Schedule 2 disc sample, the UR-SIC region was replaced with a reduced-dose (RD-SIC) region to investigate the effect of very low-temperature pre-irradiation on the corrosion behavior. Thus, the RD-SIC region was proton pre-irradiated to 2.5 dpa at –10 °C.

The results are discussed in detail in the following sections, with the principal findings summarized in Figs. 9, 10, and Table 3. Fig. 9 presents the oxide layer thicknesses measured after corrosion in the regions

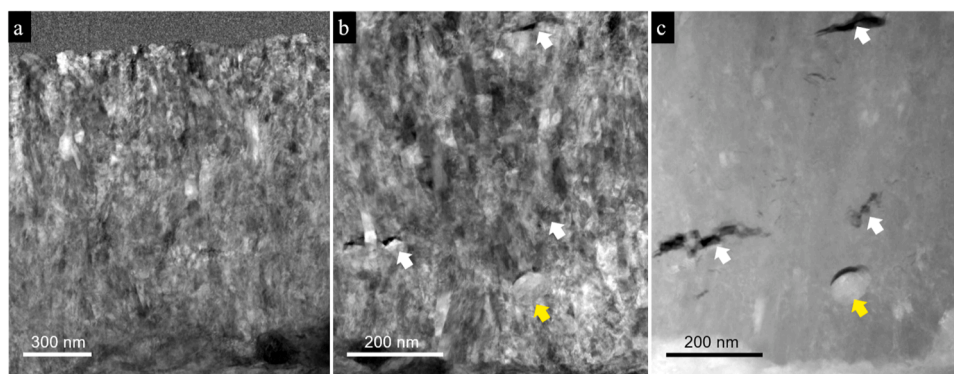


Fig. 4. TEM micrograph of two-step pre-irradiated Zircaloy-4 (#2ST-A) after 360 days of exposure in an autoclave at 320 °C. (a) brightfield image of the oxide layer displaying the columnar grains, and the oxide layer close to the metal/oxide interface where lateral cracks were developed showing in (b) brightfield mode and (c) High Angel Annular Dark Field (HAADF) mode. The white arrows denote the locations of lateral cracks within the oxide layer, while the yellow arrow indicates cracks associated with delayed-oxidized SPP [36].

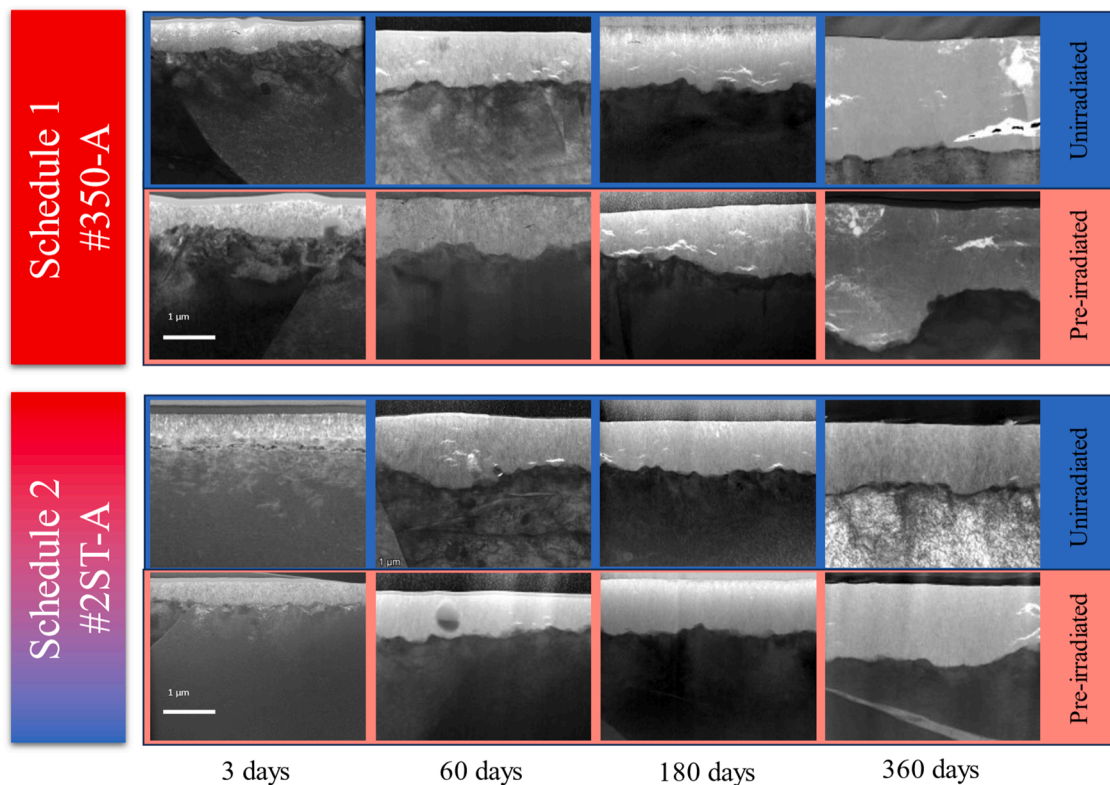


Fig. 5. TEM micrographs of oxide cross-section collected from long-term autoclave corrosion on the Schedule 1 isothermally pre-irradiated (#350-A) and Schedule 2 two-step proton pre-irradiated (#2ST-A) samples that were exposed in 320 °C pure water over 360 days.

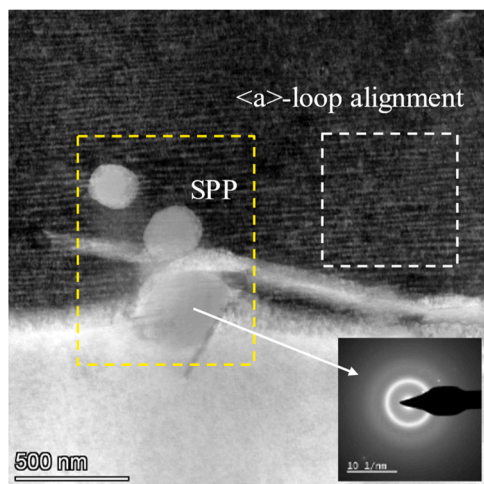


Fig. 6. STEM-ADF micrograph of the Zircaloy 2ST irradiated sample showing <a>-loop alignment in the metal and amorphized SPPs even after 360 days of autoclave exposure. The inset diffraction pattern shows the amorphous nature of the SPP.

depicted in Fig. 8, including average, minimum, and maximum values. Table 3 provides a quantitative summary of the oxide layer thicknesses. Fig. 10 displays TEM micrographs of the oxide layer cross-sections for the regions shown in Figs. 8 and 9.

Referring to the regions in Fig. 8, corrosion in Regions A and F is examined first. These samples serve as the baseline, as they were not pre-irradiated, but only subjected to the thermal heat treatments of Schedules 1 and 2, respectively. During exposure, these regions were neither subjected to SIC nor affected by radiolysis. As shown in Fig. 9 the corrosion rate in these regions was low, as also shown in Fig. 10a and e,

which show SEM micrographs indicating only a thin oxide layer with little thickness variation. The observed corrosion in Region A and F after 3 days in the SIC tests is consistent with observed corrosion on non-pre-irradiated regions after 3 days in autoclave testing.

The effect of pre-irradiation alone from either Schedule 1 or 2 on corrosion in the SIC tests is observed by comparing the corrosion in Regions B and G to that in Regions A and F, respectively. It is evident from Fig. 10b and f that pre-irradiation with either Schedule had little to no effect on the average corrosion layer thickness or the variation in oxide thickness, as the oxide layer remained thin and uniform, and similar to that seen in the autoclave tests after 3 days. Thus, neither pre-irradiation nor thermal heat treatment from either Schedule appears to have a significant impact on corrosion in the absence of SIC, as also observed in autoclave testing.

When the effect of SIC is introduced, the difference becomes apparent. The Schedule 1 sample is first examined. Region C, which is similar to Region A, underwent the thermal treatment of Schedule 1 without prior irradiation. A significant effect of SIC is evident when examining Fig. 10c– the oxide layer is an order of magnitude thicker than in Fig. 10. It exhibits a very high crack density, unlike the protective oxide layers typically observed in the literature [38–41]. The thick oxide observed in Region C shows minimal variation in thickness, as depicted in Fig. 9 and quantitatively detailed in Table 3.

Comparing Region C with Region D allows for evaluating the influence of Schedule 1 pre-irradiation on corrosion under SIC. The matrix microstructure contains black spot defects in the form of dislocation loops, but very minimal precipitation amorphization or Fe loss occurred. As shown in Fig. 10d, the average thickness of the oxide layer is about four times lower than that of Region C, but there is significant variation in the thickness of the oxide layer.

Turning now to the Schedule 2 samples, the comparison of the corrosion observed in Region F with that in Region H (RD-SIC) allows for evaluating the influence of only the first step in the two-step pre-

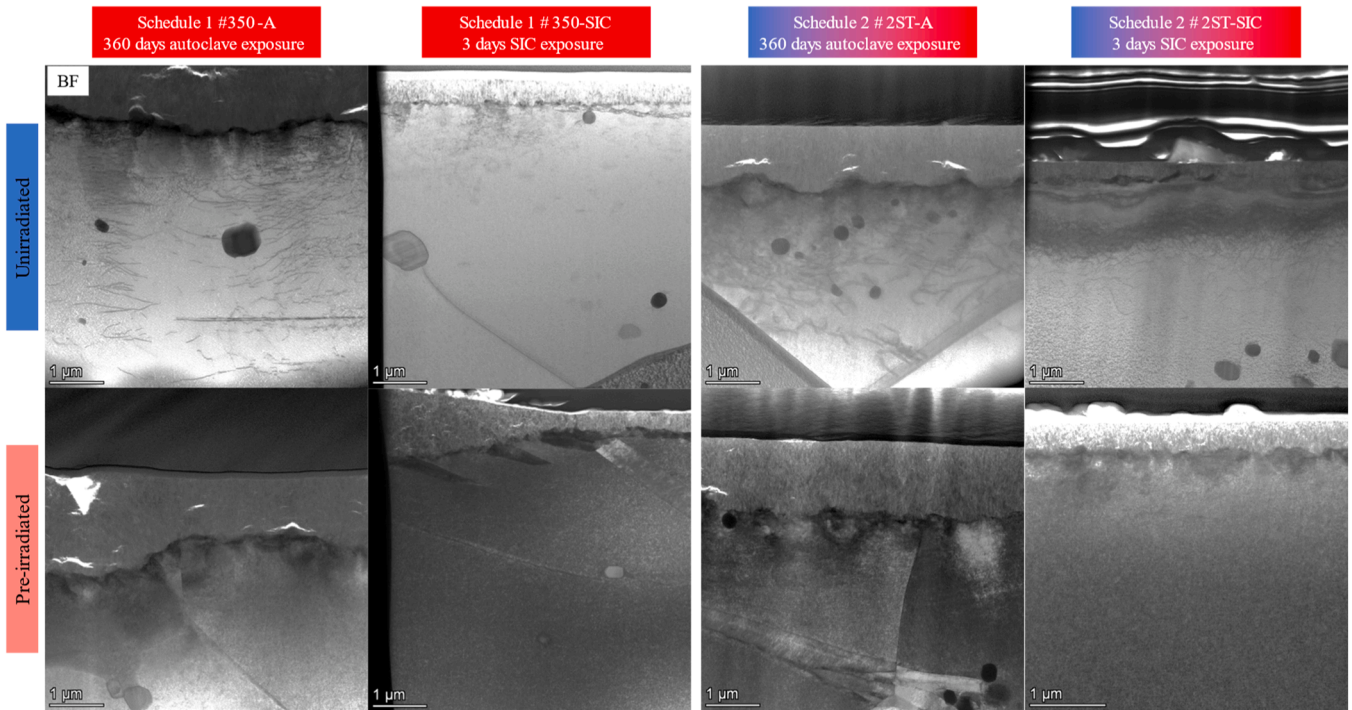


Fig. 7. STEM-BF micrographs of Zircaloy-4 metal substrate in the unirradiated condition and pre-irradiated condition.

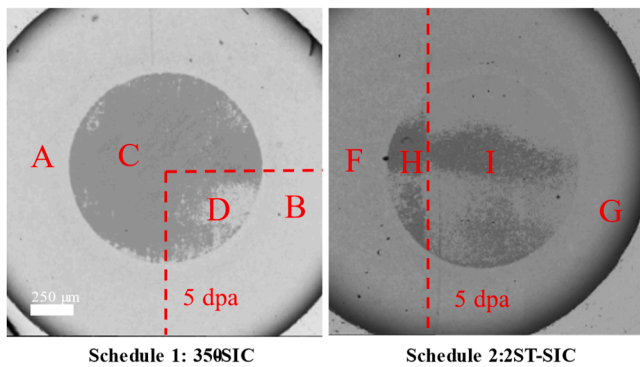


Fig. 8. SEM backscattered images of different regions in Zircaloy-4 samples submitted to SIC showing different regions. Region A is unirradiated; Region B is pre-irradiated with Schedule 1; Region C is unirradiated, subject to SIC; Region D is pre-irradiated with Schedule 1 and subject to SIC; Region F is unirradiated; Region G is pre-irradiated with Schedule 2; Region H is pre-irradiated with the first step of Schedule 2 to 2.5 dpa at $-10\text{ }^{\circ}\text{C}$, subject to SIC; Region I is pre-irradiated with Schedule 2 and subject to SIC. Under SEM backscattered conditions, light-appearing regions have a thinner corrosion film, while dark-appearing regions have a thicker corrosion film.

irradiation schedule on corrosion under SIC. The matrix microstructure contains black spot defects, and amorphized SPPs, but no Fe redistribution from the SPP. Although the average oxide thickness observed in Region H is significantly higher than that in Region F, with more variation (0.9 to 1.65 μm). When compared to Region C on the Schedule 1 disc, there is a considerable decrease in corrosion rate under SIC. As seen in Fig. 10g, the oxide layer in Region H exhibited significant variation in thickness but no clear evidence of preferential corrosion along grain boundaries or grain-to-grain preferential corrosion (Fig. 11).

The comparison of the corrosion observed in Region I with Region H and F allow for evaluating the influence of both steps in the two-step pre-irradiation schedule on corrosion. The matrix microstructure contains black spot damage, amorphized precipitates, and Fe loss from the

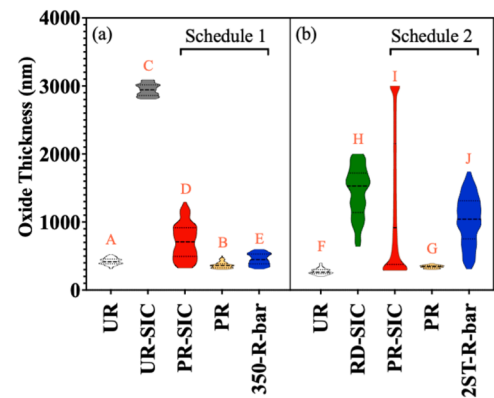


Fig. 9. Oxide thickness ranges produced in SIC experiments of Zircaloy-4 samples. The length of the marker depicts the oxide thickness range, and the width of the marker depicts the prevalence of a specific oxide thickness. Dark dashed lines depict the measured average. The Region H (RD-PR-SIC) is a reduced-dose condition for Schedule 2: 2ST-SIC sample was pre-irradiated at $-10\text{ }^{\circ}\text{C}$ for 2.5 dpa. The expected behavior of Region H (if not pre-irradiated) should be similar to Region C on Schedule 1: 350-SIC. The A-D and F-G labels refer to the Regions shown in Fig. 8.

precipitates. Fig. 10h shows the thickest region of the oxide layer formed in Region I, which is much thicker than the oxide layers formed in all other regions shown in Fig. 9b. The oxide layer exhibited a very high density of small ($\sim 0.2\text{ }\mu\text{m}$ wide) lateral cracks (several per micron), to a much higher degree than in stable protective oxides. In protective oxides, the most extensive cracking is associated with the transition [2], and thus cracks are spaced a couple of microns apart, in contrast to what is observed here. Because this high crack density is a common characteristic of the oxide layers grown under SIC conditions, it can be concluded that corrosion under SIC leads to an oxide growth process that is more unstable than in an autoclave.

Fig. 12 provides a closer view of the oxide layer formed on Region I under SIC conditions, revealing the presence of sub-micron cracks

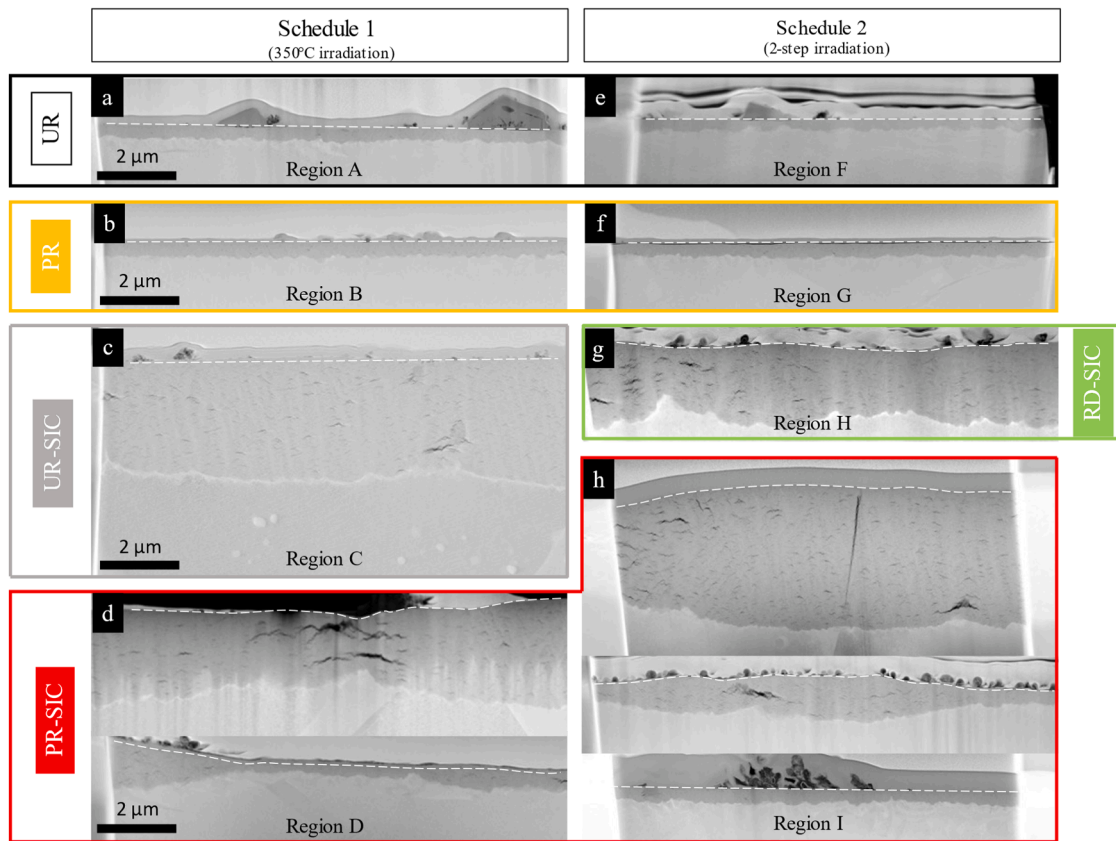


Fig. 10. STEM (HADF) micrographs of oxide cross-sections obtained from Regions A to I are listed in Table 3. The dashed line in each case mark the oxide surface.

Table 3
Summary of the SIC experimental conditions and resulting oxide thickness measurements.

Regions	Pre- irradiation	Other comments	Oxide layer thickness (microns)			SIC	Radiolysis
			Average	Minimum	Maximum		
A	None	Thermal treatment of Schedule 1 only	0.4	0.3	0.52	NO	NO
B	Schedule 1		0.33	0.29	0.55	NO	NO
C	None	Thermal treatment of Schedule 1 only	2.95	2.8	3.1	YES	YES
D	Schedule 1		0.7	0.3	1.3	YES	YES
E	Schedule 1	Radiolysis bar	0.45	0.3	0.6	NO	YES
F	None	Thermal treatment of Schedule 2 only	0.25	0.1	0.4	NO	NO
G	Schedule 2		0.35	0.3	0.4	NO	NO
H	Reduced dose Sch 2	Thermal treatment of Schedule 2	1.5	0.65	1.95	YES	YES
I	Schedule 2		0.9	0.30	3	YES	YES
J	Schedule 2	Radiolysis bar	1.05	0.3	1.75	NO	YES

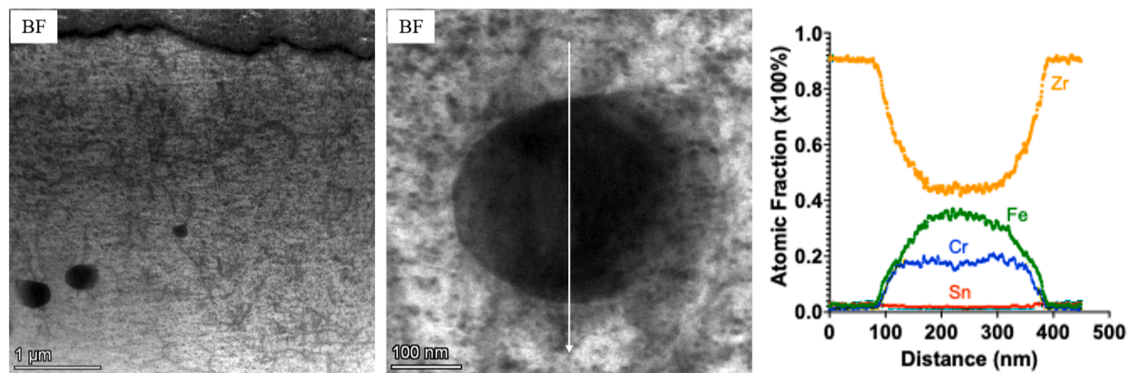


Fig. 11. STEM images of RD-SIC region from the Schedule 2 pre-irradiated disc sample. The image on the left shows the metal/oxide interface and matrix with amorphized SPPs, highlighting the alignment of features in the metal phase, e.g., black spot defects (BSD). A zoomed-in image of one of the amorphized SPPs is provided, along with its elemental profile.

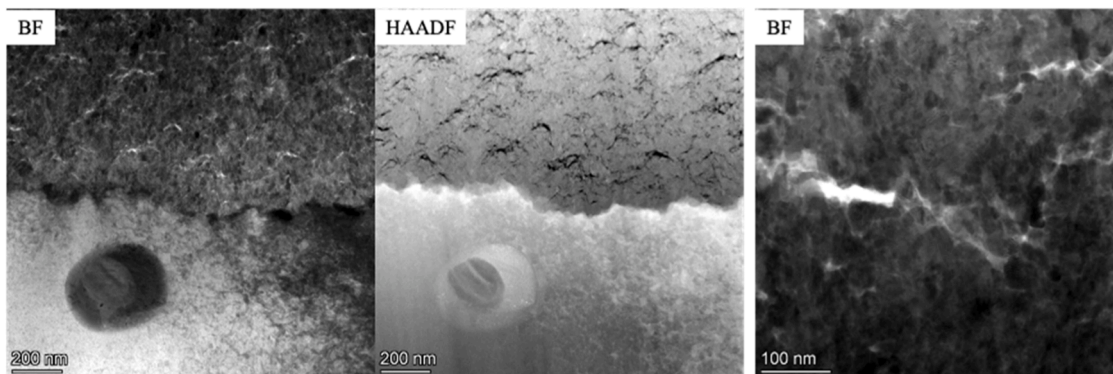


Fig. 12. STEM BF and HAADF images metal/oxide interface of Region I on Schedule 2 irradiated disc sample. The left and middle image shows the sub-micron cracks observed in the SIC-grown oxide; the right image shows the equiaxed nature of the oxide grains and nano-porosity between the grains.

throughout the oxide.

Region I formed a non-uniform nodular-like oxide where spotty patches of oxide are present on the specimen surface under back-scattered electron imaging conditions, as shown in Fig. 13. Fig. 14 shows in cross-section isolated non-uniform oxide (nodular-like) regions formed on the Schedule 2 pre-irradiated samples under SIC, leading to the high variability in corrosion thickness depicted for Region I in Fig. 9.

Finally, the corrosion observed on the radiolysis bars in Region E and Region J can be examined to highlight the effect of radiolysis without the simultaneous irradiation of the growing oxide layer under SIC. The horizontal position of the radiolysis bar hindered some of the convection flow generated by beam heating on the disc, creating a relatively stagnant region where radiolysis products accumulated on the downward-facing pre-irradiated surface. Fig. 15b and c show the different surface appearance in Region E (the radiolysis bar that saw Schedule 1 pre-irradiation) compared to Region D under SIC conditions. Regions with a thicker oxide appear darker in those micrographs. Although the thickness of the oxide layer in Region E exhibits some grain-to-grain variation, with corrosion in one grain progressing up to 2–3 times faster than in its neighboring grain. Region J (the radiolysis bar) that saw Schedule 2 pre-irradiation, shows a corrosion layer with a considerably higher degree of variation in oxide thickness (Fig. 15e and f). The oxide layer exhibits a localized corrosion, or a nodular-like pattern similar to Region I, but the upper range of the observed corrosion occurring under radiolysis alone is less than under radiolysis combined with active displacement damage. It is clear that substantial variations in oxide thickness are observed –Fig. 15f shows a factor of 5 or 6 differences in oxide thickness between regions.

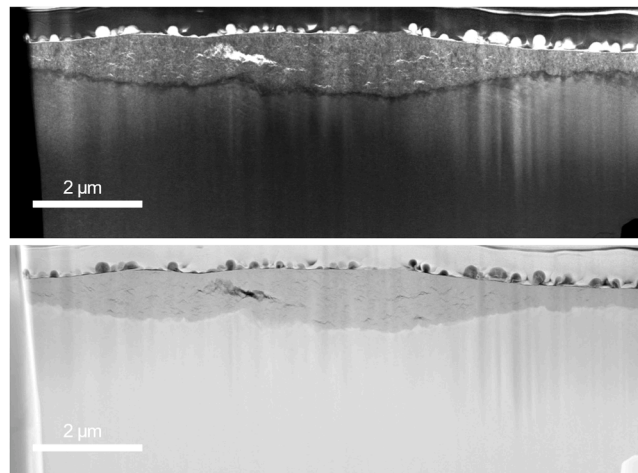


Fig. 14. Bright field and HAADF STEM images of the oxide in the PR-SIC region of the Region I #2ST-SIC sample.

4. Discussion

The results presented in the previous section help differentiate between the possible causes of corrosion acceleration of Zircaloy cladding under irradiation in a PWR. In contrast to the controlled conditions of an autoclave, corrosion within a PWR exhibits distinct differences due to

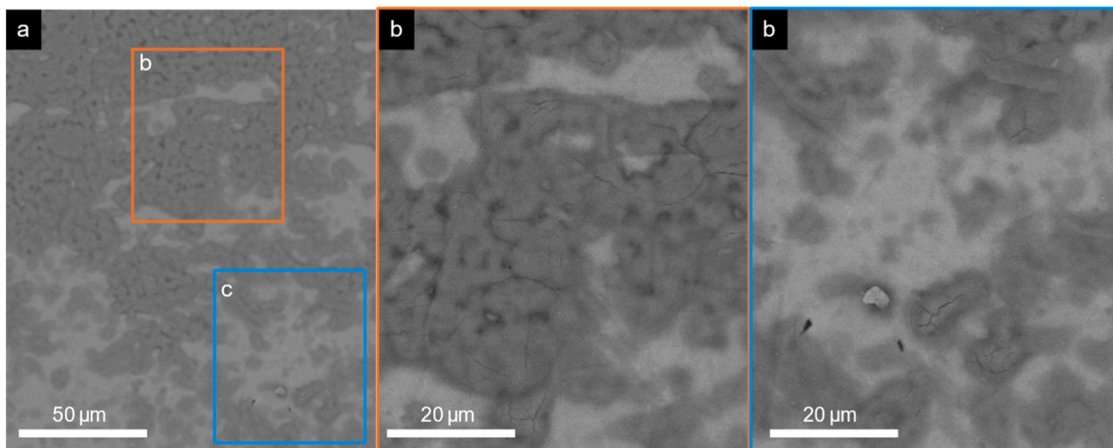


Fig. 13. Frontal backscattered SEM micrographs of (a) pre-irradiated samples subjected to SIC, subjected to Schedule 2 irradiation Region I, (b) zoomed-in region of interconnected nodules with surface cracks, (c) zoomed-in region of isolated nodules with surface cracks.

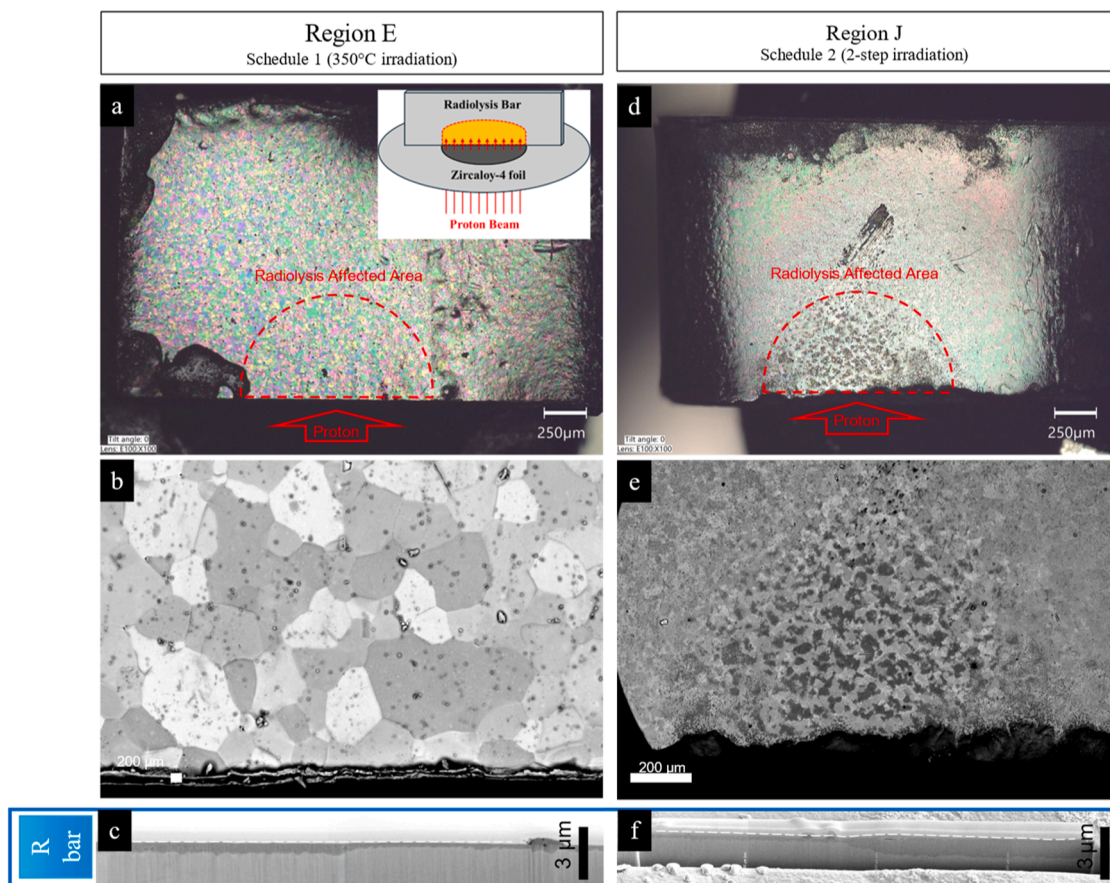


Fig. 15. The pre-irradiated radiolysis bar samples Regions E and J in (a) and (d) optical image that indicates the radiolysis-affected region as shown in the inset illustration, (b) and (e) the SEM backscattered image that shows the non-uniformity of the oxide within the radiolysis-affected region and the surrounding region with uniform oxide thickness, (c) and (f) the SEM/FIB trench cut showing the significant difference in oxide thickness between adjacent grains.

several key factors. The irradiation flux in reactors introduces displacement damage both to the substrate metal matrix and to the growing oxide layer, as well as radiolysis of the water.

This study investigates these factors by creating distinct regions that either have or have not been subjected to prior irradiation fluence, and which are or are not subjected to irradiation flux during corrosion, along with a region that experiences radiolysis alone without displacement damage during corrosion. One complicating factor that will be discussed in more detail later is that the radiolytic conditions created in the SIC tests appear to be more oxidizing than that exist in a typical PWR, approaching that of a BWR.

4.1. Impact of substrate metal irradiation damage on corrosion

Pre-irradiation does not affect corrosion in the absence of irradiation, at least in the pre-transition regime. Dislocation loop formation, amorphization of SPPs, and Fe redistribution from the SPPs appear to have little or no effect on autoclave corrosion behavior (compare autoclave exposure results on pre-irradiated samples) regardless of pre-irradiation conditions. This has also been confirmed with the out-of-flux SIC regions (compare Regions A vs. B, and F vs. G).

Radiolysis alone increases the corrosion rate on the pre-irradiated samples (compare Region E with. B, and Region J with G). However, radiolysis has a stronger effect on the sample pre-irradiated with Schedule 2 as compared to the sample pre-irradiated with Schedule 1 (compare Region J vs. E). This suggests that radiolysis combined with hardening of the matrix through irradiation defect formation (Region E) increases corrosion slightly, however, radiolysis combined with SPP amorphization and loss of Fe to the matrix increase the corrosion rate

and localize corrosion rate more substantially in the SIC test (Region J).

Concurrent ballistic damage and combined with radiolysis increase the corrosion rate even further with respect to exposure in the absence of both ballistic damage and radiolysis (compare Region C vs. A, D vs. B, H vs. F, and I vs. G). The condition of the SPPs has a strong effect on the corrosion response under SIC condition. The individual effects are discussed below:

- Schedule 1 pre-irradiation (dislocation loop formation and matrix hardening only) tends to result in more uniform corrosion behavior, while Schedule 2 pre-irradiation (dislocation loop formation, SPP amorphization and Fe loss) leads to a more heterogeneous response.
- The greatest and most uniform corrosion acceleration under SIC conditions was seen with non-pre-irradiated materials (Region C). Dislocation loop formation and concurrent matrix hardening significantly decreased that corrosion acceleration (Region D compared to Region C).
- Just amorphizing the SPPs (Schedule 2 irradiation) increases SIC corrosion over that observed with Schedule 1 irradiation induced hardening alone. (Region H compared to Region D).
- Fe loss from the amorphized SPPs then further increases SIC corrosion over that observed with amorphized SPPs alone (Region I compared to Region H).

It appears that irradiation induced matrix hardening can also be hypothesized to enhance concurrent irradiation corrosion resistance (compare Region C vs. D). According to current literature, oxide growth typically begins with the formation of small equiaxed grains. Stress minimization is achieved through the growth of columnar monoclinic

grains from properly oriented seeds [42]. The improved corrosion performance of Region D compared to Region C, suggests that strengthening of the underlying metal matrix plays a role in supporting in-plane compressive stress in the oxide, thereby stabilizing oxide growth and reducing cracking.

Oxide cracking is often associated with small, equiaxed oxide grains, as observed in previous SIC corrosion studies [20] and autoclave corrosion study [43]. The oxide formed in Region C, H and I (thicker oxide region) exhibited a higher density of lateral cracks (see Fig. 12), a characteristic feature of non-protective oxides [44].

The observed increase in oxidation rate with precipitate amorphization and Fe loss is primarily associated in these SIC tests with the onset of very non-uniform corrosion. This process can be triggered by preferential corrosion for some crystallographic orientations, where one grain corrodes faster than its neighboring grains, causing stresses at the grain boundaries [45]. These stresses can lead to oxide layer cracking, which reduces the protective nature of the oxide. Research by Ensor et al. has stated that localized corrosion can fragment the oxide layer, further destabilizing growth [46]. In Fig. 16, we hypothesize the progression of these non-uniform corrosion scenarios and connect them to our observations from both the autoclave and SIC experiments.

In summary, under the SIC conditions in these tests, the material with the least corrosion resistance is the as-manufactured, high-annealing parameter, non-pre-irradiated Zircaloy-4. Pre-irradiation, which induces dislocation loop formation and matrix hardening, considerably improves the corrosion resistance. However, pre-irradiation also causes SPP amorphization and Fe loss, which degrades corrosion resistance and can lead to highly non-uniform corrosion.

4.2. Impact of radiolysis on corrosion

The complex water chemistry under SIC conditions has a significant impact on Zircaloy-4 corrosion behavior. To assess the relevance of the current findings to PWR water chemistry conditions, the concentrations of radiolysis products generated in the SIC experiments were simulated using an adapted Python code originally developed by Doyle et al. [47], tailored to model radiolysis yield based on G-values obtained under proton radiation at 300 °C, as detailed in the review by Elliot and Bartels [48]. The simulated concentration of radiolysis products evolution as a function of time at a dose rate of 10 kGy/s (for PWR and BWR) and 72 kGy/s (for SIC tests) are depicted in Fig. 17. For simplicity, regardless of the water chemistry, the interaction time between neutron/gamma rays or protons and the water is fixed at 2 s. This duration is sufficient to

reach a steady-state and also represents the typical time required for the radiolysis products to flow out of the irradiation region during SIC tests.

In BWR environments, due to the lack of hydrogen overpressure, the dissolved oxygen levels produced in the coolant are high (typically 100–200 ppb) [49], leading to oxidizing conditions that promote high redox potentials (around 350 mV_{SHE} in normal water chemistry, BWR-NWC, and –540 mV_{SHE} in hydrogen water chemistry, BWR-HWC). These conditions generally increase the propensity for accelerated corrosion, especially in the presence of radiolysis products such as hydrogen peroxide (H₂O₂), which further elevates redox potential. At a dose rate of 10 kGy/s, which is typical for a BWR, the expected steady-state concentration of H₂O₂, O₂ and H₂ can reach up to 10 μM. Garzarolli et al. discusses the fact that Zircaloy-4 exhibits a more complex corrosion process in oxygen containing in-reactor environment, where nodular corrosion occurs on materials with annealing parameters above 10⁻¹⁸ [50]. As indicated in our previous publication, the Zircaloy-4 used in this study has an annealing parameter close to 10⁻¹⁶ [12], optimized more for PWR corrosion resistance as compared to BWR corrosion resistance.

In contrast, PWR environments operate with a hydrogen overpressure in the primary coolant and at much higher pressure (15–16 MPa), preventing boiling and leading to lower dissolution oxygen levels (typically < 5 ppb). This creates reducing conditions with much lower redox potential at –820 mV_{SHE} [49]. Water radiolysis is significantly lower compared to BWR conditions, as shown in Fig. 17. In these conditions, H₂O₂ concentration can only be sustained at 10 nM under direct neutron/gamma flux and drops to zero immediately after the radiation is removed due to scavenging effect of hydrogen on oxygen and free radicals.

In the SIC experiments, due to the higher dose rate of 72 kGy/s, significant levels of H₂O₂ are calculated to be present in the SIC region despite the use of a hydrogen overpressure. The concentration of H₂O₂ alone can reach 0.2 μM, resulting in a redox potential in the vicinity of 0 mV_{SHE} [17,51]. This increased potential is far from the typical PWR redox potential and falls somewhere between the BWR-NWC and BWR-HWC conditions. The increased corrosion potential experienced by the sample in SIC region could explain why the high annealing parameter Zircaloy-4 used in these experiments exhibited behaviors more akin to a BWR environment rather than a PWR environment in the UR-SIC position (Region C in Fig. 9). The fact that pre-irradiation improves corrosion resistance in the PR-SIC regions (Region D and I in Fig. 9) compared to the UR-SIC Region C is also consistent with high annealing parameter Zircaloy-4 in a BWR environment.

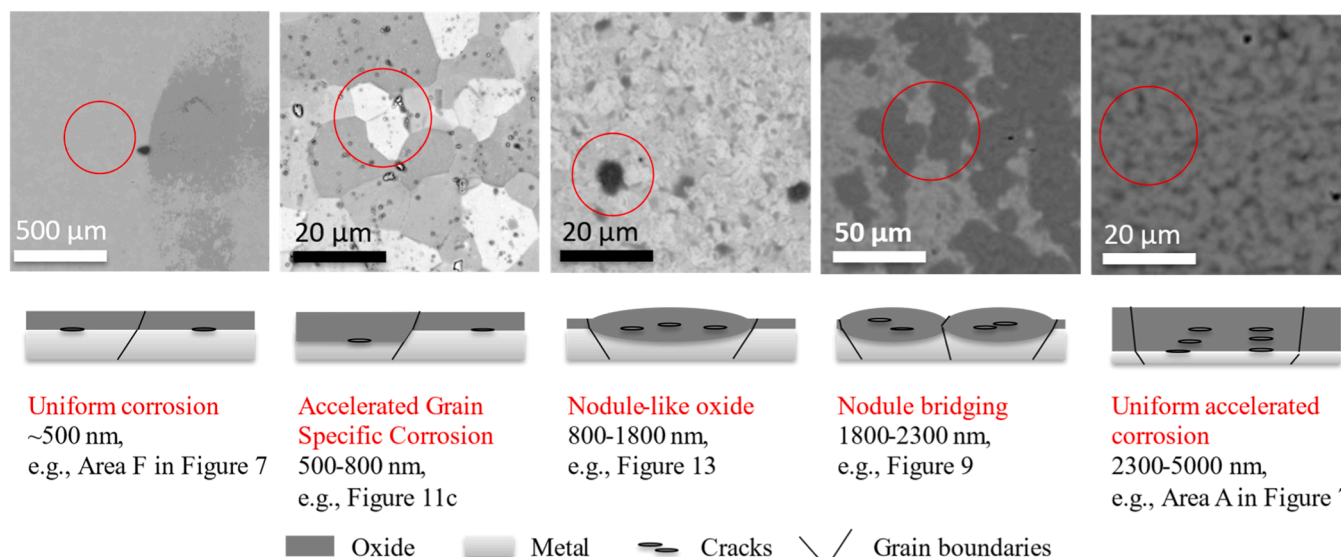


Fig. 16. Schematic of different modes of oxide localization and instability observed during autoclave and SIC experiments.

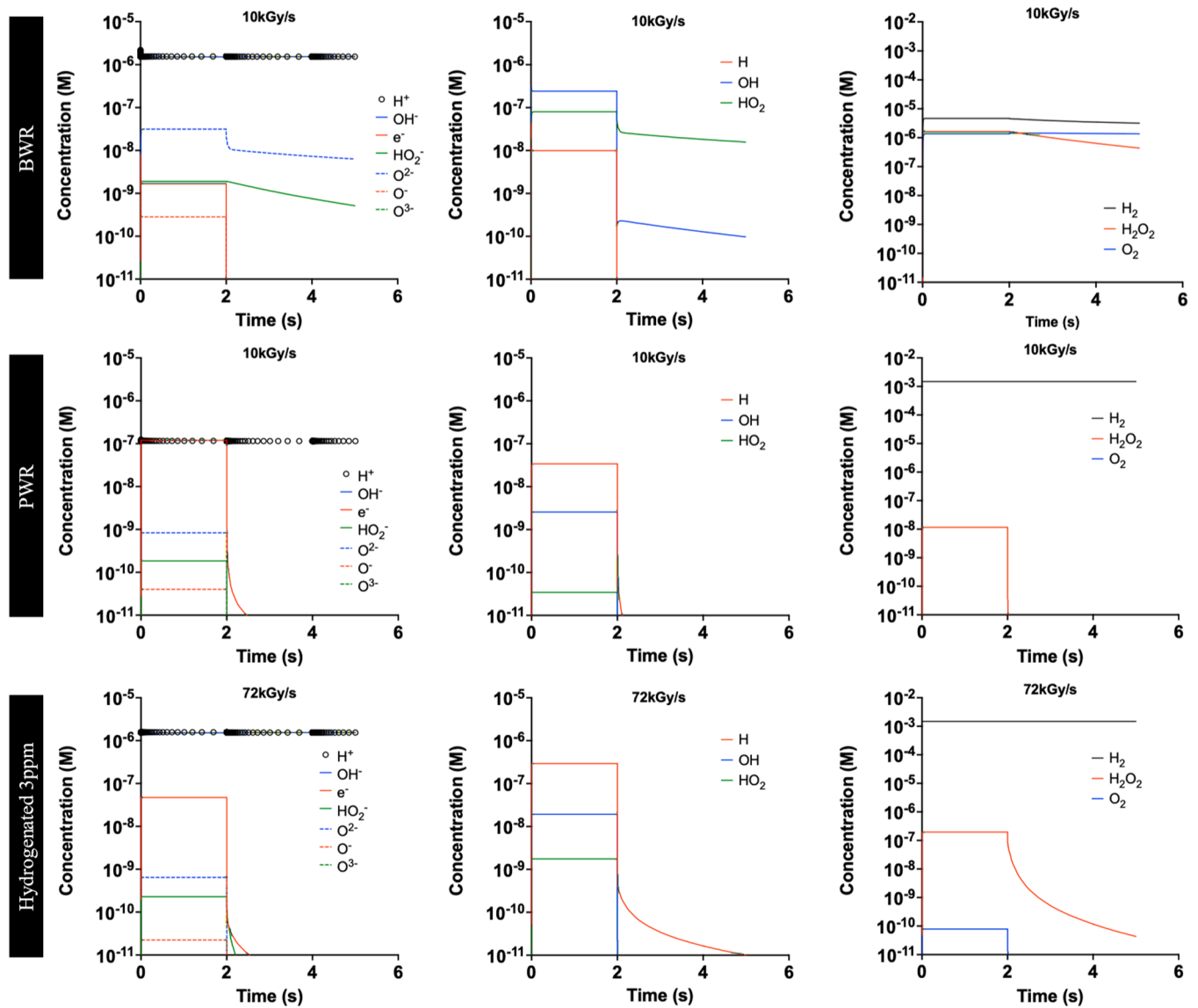


Fig. 17. Radiolysis product concentration profiles plotted as a function of time for BWR (200 ppb of dissolved oxygen) and PWR (3 ppm dissolved hydrogen) conditions at 10 kGy/s; hydrogenated water condition at 320 °C, and 72 kGy/s.

The absence of accelerated corrosion outside the SIC region, coupled with the clear boundary between the SIC and non-SIC regions in the disc samples (Fig. 8), suggests that radiolysis products in bulk water have limited reach due to their short lifespan.

4.3. Impact of active displacement damage on corrosion

Previous studies on radiation-enhanced diffusion (RED) using similar SIC test methods [18] concluded that defect recombination controls defect concentration in the oxide, and RED is not a significant mechanism for enhancing corrosion at SIC proton irradiation rates around 1×10^{-7} dpa/s. This conclusion is supported by irradiation test observation that in-PWR corrosion is not accelerated in the pre-transition corrosion regime [10]. The current tests further support this, as the damage rate during the SIC experiment was comparable to the damage rate seen in ATR studies at 310 °C at a neutron flux of approximately 6.5×10^{13} n/cm²-s, or 1×10^{-7} dpa/s [10]. Despite this similarity in damage rates, the corrosion rate in the SIC test of 1000 nm/day was 23 times higher than the corrosion rate of the ATR test at 44 nm/day under the same conditions. Even at the highest ATR neutron flux (1.6×10^{14} n/cm²-s, or 2.5×10^{-7} dpa/s), the SIC corrosion rate was 2.4 times faster, indicating

that RED in the oxide is not the primary cause of corrosion acceleration and that the higher dose rate of radiolysis in the SIC test plays a more significant role.

5. Conclusions

A detailed study was conducted to investigate the effects of irradiation on accelerating waterside corrosion in Zircaloy-4 at 320 °C using proton irradiation to simulate irradiation occurring in a light water reactor. Long-term autoclave corrosion experiments and short-term SIC tests were conducted in high-temperature water with a hydrogen overpressure on both unirradiated and pre-irradiated samples. Pre-irradiation was done following two distinct irradiation schedules. By irradiating specific regions of the samples while exposing the entire sample to high-temperature water, it became possible to discern specific effects contributing to accelerating corrosion in the SIC tests. The original goal was to investigate irradiation effects on corrosion in a PWR environment. As such, high annealing parameter Zircaloy-4 and a water environment with a hydrogen overpressure was used. The in-situ proton irradiation conditions however appears to have created a more oxidizing corrosion environment in the SIC tests than exists in the bulk channels of

a PWR. The main observations and conclusions from this testing are summarized as follows:

- Pre-irradiation does not affect corrosion in the absence of further irradiation, particularly in the pre-transition regime, as changes such as dislocation loop formation, SPP amorphization, and Fe redistribution show little effect on corrosion. This is demonstrated in both the 360-day autoclave corrosion tests and the 3-day SIC tests (comparing Region A to Region B in Fig. 9, and Region F to Region G in Fig. 9).
- Radiolysis along increases both the corrosion rate and its non-uniformity in pre-irradiated samples, with a stronger effect observed in Schedule 2 pre-irradiation (Region J in Fig. 9) compared to Schedule 1 pre-irradiation (Region E in Fig. 9). This indicates that SPP amorphization and Fe loss in Zircaloy-4 result in a more pronounced and non-uniform corrosion response in the radiolytic environment produced during SIC tests.
- Concurrent ballistic damage and radiolysis significantly accelerated corrosion compared to conditions without these effects. However, the state of the SPP plays a role in the corrosion response. Under the SIC conditions created in these tests, the least corrosion resistant material was the as-manufactured, high-annealing parameter, non-pre-irradiated Zircaloy-4 (Region C in Fig. 9). Pre-irradiation, considerably improved corrosion resistance (Region D in Fig. 9). However, when pre-irradiation also caused SPP amorphization (Region H in Fig. 9) or SPP amorphization with Fe loss (Region I in Fig. 9) corrosion resistance was degraded, leading to non-uniform corrosion.
- The fact that pre-irradiation of the Zircaloy-4 slightly improves the SIC corrosion behavior is not characteristic of a PWR corrosion environment. However, it is characteristic of a BWR corrosion environment, further supporting the radiolysis calculations that suggest the radiolytic environment in these SIC tests is more oxidizing than what typically exists in a PWR.
- Although somewhat confounded by the greater radiolysis occurring in these tests compared to the bulk channels of a typical PWR, the results suggest that the in-reactor corrosion acceleration observed in Zircaloy-4 in a PWR environment is a synergistic response to multiple factors, including irradiation-induced modifications to the base metal and the radiolytic environment at the corroding surface. The proton irradiation used in these SIC tests created a more oxidizing environment than typically found in the bulk of a PWR, even with hydrogen overpressure, supporting the possibility that heterogeneous radiolysis within a post-transition corrosion film could similarly create a more oxidizing environment than exists in the bulk coolant channels of a PWR.

CRedit authorship contribution statement

Peng Wang: Writing – original draft, Writing – review & editing, Visualization, Validation, Methodology, Investigation, Formal analysis, Data curation. **Bruce Kammenzind:** Writing – review & editing, Funding acquisition, Conceptualization, Project administration, Resources. **Richard Smith:** Writing – review & editing, Funding acquisition, Investigation. **Arthur Motta:** Writing – review & editing, Investigation, Supervision, Funding acquisition. **Matthieu Aumand:** Writing – review & editing, Funding acquisition. **Damien Kaczorowski:** Writing – review & editing, Funding acquisition. **Mukesh Bachhav:** Writing – review & editing, Visualization, Data curation. **Gary Was:** Writing – review & editing, Supervision, Project administration, Funding acquisition, Investigation, Conceptualization, Methodology, Resources.

Declaration of competing interest

The authors declare that they have no known competing financial

interests or personal relationships that could have appeared to influence the work reported in this paper.

Acknowledgment

This study was supported by Fluor Marine Propulsion, LLC., under contract No. DOE-89233018CNR000004 with the U.S. Department of Energy (DOE). We gratefully acknowledge the Michigan Ion Beam Laboratory, High-Temperature Corrosion Laboratory, and Michigan Center for Materials Characterization at the University of Michigan for their invaluable contributions to this paper through state-of-the-art experimental capabilities and robust data collection. Mukesh Bachhav is supported through the INL Laboratory Directed Research & Development (LDRD) Program under DOE Idaho Operation Office Contract DE-AC07–05ID14517. Additionally, the research described in this manuscript was conducted as part of the MUZIC (Mechanistic Understanding of Zr Alloy Corrosion)–3 project.

Data availability

Data will be made available on request.

References

- [1] P. Tejland, H.-O. Andrén, Origin and effect of lateral cracks in oxide scales formed on zirconium alloys, *J. Nucl. Mater.* 430 (2012) 64–71, <https://doi.org/10.1016/j.jnucmat.2012.06.039>.
- [2] A. Yilmazbayhan, A.T. Motta, R.J. Comstock, G.P. Sabol, B. Lai, Z. Cai, Structure of zirconium alloy oxides formed in pure water studied with synchrotron radiation and optical microscopy: relation to corrosion rate, *J. Nucl. Mater.* 324 (2004) 6–22, <https://doi.org/10.1016/j.jnucmat.2003.08.038>.
- [3] B. Cox, Some thoughts on the mechanisms of in-reactor corrosion of zirconium alloys, *J. Nucl. Mater.* 336 (2005) 331–368, <https://doi.org/10.1016/j.jnucmat.2004.09.029>.
- [4] P. Bossis, F. Lefebvre, P. Barberis, A. Galerie, Corrosion of zirconium alloys: the link between the metal/oxide interface roughness, the degradation of the protective oxide layer and the corrosion kinetics, in: *Materials Science Forum*, 2001. 10.4028/www.scientific.net/msf.369-372.255.
- [5] IAEA, P. Billot, B. Cox, K. Ishigure, A.B. Johnson, C. Lemaignan, A.F. Nechaev, N. G. Petrik, E.A. Reznichenko, I.G. Ritchi, G.I. Sukhanov, *Corrosion of Zirconium Alloys in Nuclear Power Plants* (1993).
- [6] E. Hillner, *Corrosion of zirconium-base alloys? An overview. Zirconium in the Nuclear Industry*, ASTM International, 1977.
- [7] F. Garzarolli, R. Manzel, S. Reschke, E. Tenckhoff, Review of corrosion and dimensional behavior of Zircaloy under water reactor conditions, in: *ASTM Special Technical Publication*, 1979: pp. 91–106. 10.1520/stp36674s.
- [8] F. Garzarolli, D. Jorde, R. Manzel, J.R. Politano, P.G. Smerd, *Waterside Corrosion of Zircaloy-Clad Fuel Rods in a PWR Environment*, ASTM Special Technical Publication, 1982, pp. 430–449, <https://doi.org/10.1520/stp37065s>. D.G. Franklin.
- [9] IAEA, *Waterside corrosion of zirconium alloys in nuclear power plants*, IAEA-TECDOC-996 (1998).
- [10] B.F. Kammenzind, J.A. Gruber, R. Bajaj, J.D. Smeed, Neutron irradiation effects on the corrosion of Zircaloy-4 in a pressurized water reactor environment, in: *Proceedings of the Zirconium in the Nuclear Industry: 18th International Symposium*, ASTM International, 2018, pp. 448–490, <https://doi.org/10.1520/STP159720160085>, 100 Barr Harbor Drive, PO Box C700, West Conshohocken, PA 19428-2959.
- [11] D.M. Rishel, B.F. Kammenzind, The role of gamma radiation on Zircaloy-4 corrosion. *ASTM Special Technical Publication*, ASTM International, 2018, pp. 555–595, <https://doi.org/10.1520/STP159720160029>, 100 Barr Harbor Drive, PO Box C700, West Conshohocken, PA 19428-2959.
- [12] P. Wang, J. Bowman, M. Bachhav, B. Kammenzind, R. Smith, J. Carter, A. Motta, E. Lacroix, G. Was, Emulation of neutron damage with proton irradiation and its effects on microstructure and microchemistry of Zircaloy-4, *J. Nucl. Mater.* 557 (2021) 153281, <https://doi.org/10.1016/j.jnucmat.2021.153281>.
- [13] R. Bajaj, B.F. Kammenzind, D.M. Farkas, Effects of neutron irradiation on the microstructure of alpha-annealed Zircaloy-4. *ASTM Special Technical Publication*, ASTM International, 2002, pp. 400–425, <https://doi.org/10.1520/stp11399s>, 100 Barr Harbor Drive, PO Box C700, West Conshohocken, PA 19428-2959.
- [14] M. Griffiths, R.W. Gilbert, G.J.C. Carpenter, Phase instability, decomposition and redistribution of intermetallic precipitates in Zircaloy-2 and -4 during neutron irradiation, *J. Nucl. Mater.* 150 (1987) 53–66, [https://doi.org/10.1016/0022-3115\(87\)90093-6](https://doi.org/10.1016/0022-3115(87)90093-6).
- [15] J. Ziegler, M. Ziegler, J. Biersack, *SRIM - The Stopping and Range of Ions in Matter*, SRIM Co., 2008.
- [16] S.S. Raiman, A. Flick, O. Toader, P. Wang, N.A. Samad, Z. Jiao, G.S. Was, A facility for studying irradiation accelerated corrosion in high temperature water, *J. Nucl. Mater.* 451 (2014) 40–47, <https://doi.org/10.1016/j.jnucmat.2014.03.022>.

- [17] P. Wang, S. Grdanovska, D.M. Bartels, G.S. Was, Effect of radiation damage and water radiolysis on corrosion of FeCrAl alloys in hydrogenated water, *J. Nucl. Mater.* 533 (2020) 152108, <https://doi.org/10.1016/j.jnucmat.2020.152108>.
- [18] M. Reyes, P. Wang, G. Was, J. Marian, Determination of dose rate effects on Zircaloy oxidation using proton irradiation and oxygen transport modeling, *J. Nucl. Mater.* 523 (2019) 56–65, <https://doi.org/10.1016/j.jnucmat.2019.05.039>.
- [19] K. Fukuya, Current understanding of radiation-induced degradation in light water reactor structural materials, *J. Nucl. Sci. Technol.* 50 (2013) 213–254, <https://doi.org/10.1080/00223131.2013.772448>.
- [20] P. Wang, G.S. Was, Oxidation of Zircaloy-4 during in situ proton irradiation and corrosion in PWR primary water, *J. Mater. Res.* 30 (2015) 1335–1348, <https://doi.org/10.1557/jmr.2014.408>.
- [21] P. Wang, K. Nowotka, G.S. Was, Reproducing shadow corrosion on Zircaloy-2 using in-situ proton irradiation, *J. Nucl. Mater.* 558 (2022) 153406, <https://doi.org/10.1016/j.jnucmat.2021.153406>.
- [22] M. Griffiths, A review of microstructure evolution in zirconium alloys during irradiation, *J. Nucl. Mater.* 159 (1988) 190–218, [https://doi.org/10.1016/0022-3115\(88\)90093-1](https://doi.org/10.1016/0022-3115(88)90093-1).
- [23] Y.P. Lin, D.W. White, D.R. Lutz, Effects of Chemistry and Microstructure on Corrosion Performance of Zircaloy-2-Based BWR Cladding, ASTM Special Technical Publication, 2018, <https://doi.org/10.1520/STP159720160066>.
- [24] S. Yagnik, R.B. Adamson, G. Koblyansky, J.H. Chen, D. Gilbon, S. Ishimoto, T. Fukuda, L. Hallstadius, A. Obukhov, S. Mahmood, Effect of Alloying elements, Cold work, and Hydrogen on the Irradiation-Induced Growth Behavior of Zirconium Alloy Variants, ASTM Special Technical Publication, 2018, <https://doi.org/10.1520/STP159720160040>.
- [25] B. Ensor, G. Lucadamo, J.R. Seidensticker, R. Bajaj, Z. Cai, A.T. Motta, Characterization of Long-Term, In-Reacto Zircaloy-4 Corrosion Coupons and the Impact of Flux, Fluence, and Temperature on Oxide Growth, Stress Development, Phase Formation, and Grain Size, ASTM Special Technical Publication, 2021, <https://doi.org/10.1520/STP162220190038>.
- [26] F. Garzarolli, P. Dewes, G. Maussner, H.-H. Basso, Effects of High Neutron Fluences on Microstructure and Growth of Zircaloy-4, American Society for Testing and Materials, Philadelphia, 1989, pp. 641–657, <https://doi.org/10.1520/stp18891s>. L. E. E. Van Swam, C. M. Eucken Zirconium in the Nuclear Industry: Eighth International Symposium.
- [27] C. Coleman, P. Chow, C. Eells, M. Griffiths, E. Ibrahim, S. Sagat, Rejuvenation of fracture properties of irradiated Zr-2.5 Nb by heat treatment, in: R.E. Stoller, A. S. Kumar, D.S. Gelles (Eds.), Proceedings of the Effects of Radiation on Materials: 15th International Symposium, ASTM International, 1992, <https://doi.org/10.1520/STP17877S>, 100 Barr Harbor Drive, PO Box C700, West Conshohocken, PA 19428-2959.
- [28] S.T. Mahmood, D.M. Farkas, R.B. Adamson, Y. Etoh, Post-irradiation characterization of ultra-high-fluence Zircaloy-2 plate. ASTM Special Technical Publication, ASTM International, 2000, pp. 139–169, <https://doi.org/10.1520/stp14299s>, 100 Barr Harbor Drive, PO Box C700, West Conshohocken, PA 19428-2959.
- [29] D. Gilbon, A. Soniak, S. Doriot, J.P. Mardon, Irradiation Creep and Growth Behavior, and Microstructural Evolution of Advanced Zr-base Alloys, ASTM Special Technical Publication, 2000, <https://doi.org/10.1520/stp14294s>.
- [30] C.M. Eucken, P.T. Finden, S. Trapp-Pritsching, H.G. Weidinger, Influence of chemical composition on uniform corrosion of zirconium-base alloys in autoclave tests, in: Proceedings of the Zirconium in the Nuclear Industry: Eighth International Symposium, 1989.
- [31] R.A. Graham, J.P. Tosdale, P.T. Finden, Influence of chemical composition and manufacturing variables on autoclave corrosion of the Zircalloys, in: Proceedings of the Zirconium in the Nuclear Industry: Eighth International Symposium, 1989.
- [32] E. Hillner, D.G. Franklin, J.D. Smeed, Long-term corrosion of Zircaloy before and after irradiation, *J. Nucl. Mater.* 278 (2000) 334–345.
- [33] A.T. Motta, M.J.G. Da Silva, A. Yilmazbayhan, R.J. Comstock, Z. Cai, B. Lai, Microstructural characterization of oxides formed on model Zr alloys using synchrotron radiation, *J. ASTM Int.* (2008), <https://doi.org/10.1520/JAI101257>.
- [34] W.J.S. Yang, R.P. Tucker, B. Cheng, R.B. Adamson, Precipitates in Zircaloy: identification and the effects of irradiation and thermal treatment, *J. Nucl. Mater.* 138 (1986) 185–195, [https://doi.org/10.1016/0022-3115\(86\)90005-X](https://doi.org/10.1016/0022-3115(86)90005-X).
- [35] H.R. Peters, Improved Characterization of Aqueous Corrosion Kinetics of Zircaloy-4, American Society for Testing and Materials, 1984, pp. 507–518, <https://doi.org/10.1520/stp34489s>. D.G. Franklin, R.B. Adamson ASTM STP0824.
- [36] M. Blat, L. Legras, D. Noel, H. Amanrich, Contribution to a Better Understanding of the Detrimental Role of Hydrogen on the Corrosion Rate of Zircaloy-4 Cladding Materials, ASTM Special Technical Publication, 2000, <https://doi.org/10.1520/stp14317s>.
- [37] E. Hillner, Hydrogen Absorption in Zircaloy During Aqueous Corrosion, Effect of Environment, AEC Research and Development, 1964.
- [38] A. Shevyakov, V.V. Novikov, V.A. Markelov, A.V. Obukhov, G.P. Koblyansky, Study of structure-phase state of oxide films on E110 and E635 alloys at pre- and post-irradiation stages, in: Proceedings of the Zirconium in the Nuclear Industry: 18th International Symposium, ASTM International, 2018, pp. 596–613, <https://doi.org/10.1520/STP159720160064>, 100 Barr Harbor Drive, PO Box C700, West Conshohocken, PA 19428-2959.
- [39] A. Garner, F. Baxter, P. Frankel, M. Topping, A. Harte, T. Slater, P. Tejlund, J. E. Romero, E.C. Darby, A. Cole-Baker, M. Gass, M. Preuss, Investigating the effect of zirconium oxide microstructure on corrosion performance: a comparison between neutron, proton, and nonirradiated oxides, in: Proceedings of the Zirconium in the Nuclear Industry: 18th International Symposium, ASTM International, 2018, pp. 491–523, <https://doi.org/10.1520/STP159720160069>, 100 Barr Harbor Drive, PO Box C700, West Conshohocken, PA 19428-2959.
- [40] A. Yilmazbayhan, E. Breval, A.T. Motta, R.J. Comstock, Transmission electron microscopy examination of oxide layers formed on Zr alloys, *J. Nucl. Mater.* 349 (2006) 265–281, <https://doi.org/10.1016/j.jnucmat.2005.10.012>.
- [41] N. Ni, D. Hudson, J. Wei, P. Wang, S. Lozano-Perez, G.D.W.D.W. Smith, J.M. M. Sykes, S.S.S. Yardley, K.L.L. Moore, S. Lyon, R. Cottis, M. Preuss, C.R.M.R. M. Grovener, How the crystallography and nanoscale chemistry of the metal/oxide interface develops during the aqueous oxidation of zirconium cladding alloys, *Acta Mater.* 60 (2012) 7132–7149, <https://doi.org/10.1016/j.actamat.2012.09.021>.
- [42] Y. Etoh, Effects of operational parameters on nodular lorrison characteristics, *J. Nucl. Sci. Technol.* 26 (1989), <https://doi.org/10.1080/18811248.1989.9734379>.
- [43] B. De Gabory, A.T. Motta, K. Wang, Transmission electron microscopy characterization of Zircaloy-4 and ZIRLO™ oxide layers, *J. Nucl. Mater.* 456 (2015) 272–280, <https://doi.org/10.1016/j.jnucmat.2014.09.073>.
- [44] A. Motta, A. Yilmazbayhan, R. Comstock, J. Partezana, G. Sabol, B. Lai, Z. Cai, Microstructure and growth mechanism of oxide layers formed on Zr alloys studied with micro-beam synchrotron radiation, in: Proceedings of the Zirconium in the Nuclear Industry: Fourteenth International Symposium, ASTM International, 2005, <https://doi.org/10.1520/STP37508S>, 100 Barr Harbor Drive, PO Box C700, West Conshohocken, PA 19428-2959.
- [45] M.S. Yankova, A. Garner, F. Baxter, S. Armsen, C.P. Race, M. Preuss, P. Frankel, Untangling competition between epitaxial strain and growth stress through examination of variations in local oxidation, *Nat. Commun.* 14 (2023), <https://doi.org/10.1038/s41467-022-35706-3>.
- [46] B. Ensor, A.T. Motta, A. Lucente, J.R. Seidensticker, J. Partezana, Z. Cai, Investigation of breakaway corrosion observed during oxide growth in pure and low alloying element content Zr exposed in water at 360°C, *J. Nucl. Mater.* 558 (2022), <https://doi.org/10.1016/j.jnucmat.2021.153358>.
- [47] P. Doyle, K. Sun, L. Snead, Y. Katoh, D. Bartels, S. Zinkle, S. Raiman, The effects of neutron and ionizing irradiation on the aqueous corrosion of SiC, *J. Nucl. Mater.* 536 (2020), <https://doi.org/10.1016/j.jnucmat.2020.152190>.
- [48] A.J. Elliot, D.M. Bartels, The Reaction Set, Rate Constants and G-Values For the Simulation of the Radiolysis of Light Water Over the Range 20 to 350°C Based on Information Available in 2008, Atomic Energy of Canada Limited, Chalk River, Ontario, Canada, 2009. Report AECL No. 153-127160-450-001, http://inis.iaea.org/search/search.aspx?orig_q=RN:41057263.
- [49] K.A. Terrani, Y. Yang, Y. Kim, R. Rebak, H.M.M. Iii, T.J. Gerczak, Hydrothermal corrosion of SiC in LWR coolant environments in the absence of irradiation *, *J. Nucl. Mater.* 465 (2015) 488–498, <https://doi.org/10.1016/j.jnucmat.2015.06.019>.
- [50] F. Garzarolli, E. Steinberg, H.G. Weidinger, Microstructure and corrosion studies for optimized PWR and BWR Zircaloy cladding, in: Proceedings of the Zirconium in the Nuclear Industry: Eighth International Symposium, 1989.
- [51] P. Wang, S. Grdanovska, D.M. Bartels, G.S. Was, Corrosion behavior of ferritic FeCrAl alloys in simulated BWR normal water chemistry, *J. Nucl. Mater.* 545 (2021) 152744, <https://doi.org/10.1016/j.jnucmat.2020.152744>.